Article

Modelling of Powder Removal for Additive Manufacture Postprocessing

Andrew Roberts [1] Recep Kahraman [2], Desi Bacheva [2], and Gavin Tabor [1,*] https://orcid.org/0000-0003-3549-228X

[1] CEMPS, University of Exeter, Harrison Building, North Park Road, Exeter EX4 4QF.
[2] HiETA Technologies Ltd, Bristol and Bath Science Park, Dirac Crescent, Emersons Green, Bristol BS16 7FR.
* Correspondence: g.r.tabor@ex.ac.uk; Tel.: +44-1392-723662

Abstract: A critical challenge underpinning the adoption of Additive Manufacture (AM) as a technology is the postprocessing of manufactured components. For Selective Laser Sintering (SLS) this can involve the removal of powder from the interior of the component, often by vibrating the component to fluidise the powder to encourage drainage. In this paper we develop and validate a computational model of the flow of metal powder suitable for predicting powder removal from such AM components. The model is a continuum Eulerian multiphase model of the powder including models for the granular temperature; the effect of vibration can be included through appropriate wall boundaries for this granular temperature. We validate the individual sub-models appropriate for AM metal powders by comparison with in-house and literature experimental results, and then apply the full model to a more complex geometry typical of an AM Heat Exchanger. The model is shown to provide valuable and accurate results at a fraction of the computational cost of a particle-based model.

Keywords: Selective Laser Sintering; Metal powder manufacturing; post processing; Eulerian model; Computational Fluid Dynamics; granular flow

Citation: Roberts, A; Kahraman, R.; Bacheva, D,; Tabor, G. Modelling of Powder Removal for Additive Manufacture Postprocessing. *Journal Not Specified* **2021**, *1*, 0. https://dx.doi.org/10.3390/1010000

Received:
Accepted:
Published:

1. Introduction

Powder bed fusion methods are one of the main groups of Additive Manufacturing methods appropriate for metal forming. In these processes, successive layers of fine metal powder are layered on the manufacturing bed and fused together, for example using high power lasers (selective laser sintering or SLS). This can produce high resolution features including internal structures such as tubes and ducts, and challenging internal geometries which cannot be synthesised except through AM. A wide range of metal alloys are suitable for this sort of processing; in general any metal that can be welded can be used for SLS. SLS can of course also be used for other materials, including polymers and ceramics.

These methods however do present challenges as well, one of which is the removal of the surplus powder from the finished product. This will be particularly challenging when the product design includes interior structures such as fine tubes for compact heat exchangers or cooling ducts for gas turbine blades. In these cases, effective and complete powder removal is a requirement if the component is to function correctly, whilst at the same time redesign of the component to facilitate powder removal in postprocessing may not be desirable. Furthermore, the economic viability of producing large numbers of parts using powder bed systems depends heavily on the reduction of recurring costs [1]. Fine metal powders in powder bed systems can be costly, so waste should be avoided [2].

The surplus powder trapped inside the component can most conveniently be removed using vibrating systems [3]. Vibrating the component at high frequency or at the natural frequency of the component will fluidise the powder allowing it to flow out under gravity, similar to the process used for vibratory shake-outs in sand casting [4] [5]. However this process has rarely been analysed in any detail. It is particularly critical with the complex components now being developed such as compact heat exchangers, which may require a complex series of vibratory manipulations to fully remove all surplus powder and where

 doi:10.20944/preprints202106.0688.v1

any residual powder within the heat exchanger will substantially degrade performance. It is therefore essential to establish computational modelling techniques designed to predict powder flows for post-processing in powder bed additive layer manufacturing.

1.1. Granular Flow

Flow of fluidised metal powders is a problem of granular flow. This is an important physical problem with a range of industrial applications, and so has been extensively studied in the past. The basic element of the physics involves particle-particle interaction, which can therefore be evaluated through Newton's laws of motion; however when the number of particles involved becomes very large, this may become unwieldy, in which case continuum mechanics approaches may be preferred. However this is complicated by the fact that the individual particle-particle interactions may not be perfectly elastic. Whilst for fluid dynamics the Navier-Stokes equations can be derived as the continuum limit of the Boltzmann transport equation for molecular dynamics, for granular flow, due to the complexity of the physical interactions there is no equivalent set of constitutive equations that can adequately represent the range of observed behaviour. Instead, empirical constitutive relations have been identified and used [6], particularly in engineering applications.

Empirically there are various regimes which can be identified in granular flow [7,8]:

- Quasi-static or granular solid or elastic-quasi-static
- Dense or granular liquid or elastic-inertial
- Dilute or granular gas or inertial (also known as rapid granular flow)

In quasi-static flow a densely packed bed of particles is sheared at a low rate and stress is independent of the shear rate. For dense flows, multiple and enduring contacts are dominant and stress is proportional to the shear rate. Dilute flows are characterised by binary and instantaneous collisions and the stress is proportional to the square of the shear rate [7], the so-called Bagnold flow [9]. The all important flow is the dense granular flow. This is an observation from real-life, in the sense that hoppers, reasonably deep chute flows and commercial scale vibrated boxes all operate in a near packed state [10].

1.2. Computational Modelling of Granular Flow

Computational work used to describe contact forces can be classified into the following categories [11].

- Microscopic models and particle based simulations
- Statistical mechanics and kinetic theories
- Continuum and phenomenological models

As can be seen this covers the full range of scales in the flow problem. Multi-scale simulations [12,13] can combine several approaches such as Discrete Element Models (DEM) with Finite Element (FE) or Finite Volume (FV) continuum models in the same simulation. The FE/FV is employed to solve a boundary value problem, while using the DEM to derive the required nonlinear material responses at each Gauss integration point. Despite this, multi-scale approaches should not elude a theoretical micromechanical approach with the goal of basing macrosopic models on internal variables pertaining to the granular texture for a better understanding of the origins of the complex phenomenology of granular materials [14]. In this endeavor, continuum mechanics provides the framework for a rational analysis but the shift towards multiscale modeling is unavoidable. The question is how much of the rich information obtained at the microscale is relevant to the macrobehavior [14]. To this end, molecular dynamics and continuum approaches are reviewed in this section.

1.2.1. Particle-based Modelling

Particle based models are based on the lagrangian tracking of individual particles within the flow, and comprise both molecular dynamics models (MDM) and Discrete Element models (DEM); the main distinction between these being that MDM uses point particles whilst DEM considers finite size particles and includes the effects of shape and

 doi:10.20944/preprints202106.0688.v1

rotational degrees of freedom on their dynamics. As can be appreciated these additional physical parameters can be of significant importance in assessing the behaviour of metal powders in SLS, and so DEM has frequently been applied to advance our understanding of the technique; see section 1.3 for further details.

In implementation these methods are usually either soft-particle methods or event-driven methods. Soft-particle methods are relatively slow and used mostly for the analysis of dense flows when generally faster event-driven algorithms are not applicable [15]. While event-driven methods are typically faster for dilute rapid granular flows, they become impractical for dense flows in which collisions are very frequent and, furthermore, particles develop persistent contacts [15]. However both methods are computationally costly when modelling very large numbers of particles.

1.2.2. Continuum Modelling

In parallel to the development of DEM for granular flow, the Computational Fluid Dynamics community has developed a range of techniques for dispersed multiphase flow modelling, which can be applied to high phase fraction flows with solid particles, appropriate for fluidised beds. These include Lagrangian particle tracking, in which the individual particles are tracked through the solution of NII for each particle (sometimes through coupling with a DEM code) or alternatively through the use of Eulerian-Eulerian (Eulerian Multiphase) modelling, where the dispersed secondary phase is modelled through a separate set of continuum mechanics equations.

The Eulerian-Lagrangian approach has some advantages for predicting particulate flows in which large particle accelerations occur. It can also model particulate two-phase flows consisting of polydispersed particle size distributions. The Eulerian-Eulerian approach seems to have advantages in all flow cases where high particle concentrations occur and where the high void fraction of the flow becomes a dominating flow controlling parameter [16].

The $\mu(I)$ rheology for granular flows is only accurate for inertial numbers of less than around 0.3 [17] [18], which limits its application to dense or liquid-like flows, in other words gas-like behaviour at high inertial numbers cannot be modelled. For solid modelling in the $\mu(I)$ rheology, the use of a simple Coulomb friction model for the flow threshold is also a limitation and the complex transition between solid-like and liquid-like behaviour is ignored, such as shear bands, intermittent flows and hysteresis [19].

Eulerian-Eulerian models for gas-particle flows are practical for industrial systems as they balance CPU cost with simulation accuracy [20]. In many gas-particle flows of industrial significance, one can find regions in the flow domain where kinetic stresses dominate, other regions where frictional stresses dominate and finally, regions where contributions of both are comparable. Thus, it is of practical interest to synthesize rheological models that combine the frictional and kinetic contributions [21].

Often DEM and continuum FE can be applied to similar systems and gain equivalent results, such as for a particle hopper (conical hopper simulated with FEA [22], flat bottom hopper simulated with DEM [23]). Direct comparisons, where they have been done, show the hardly surprising result that whilst DEM can more detailed [24], FEA is computationally much less costly [25], taking only hours to compute as against days for DEM.

1.3. Powder Flow Modelling for AM

DEM has seen extensive application in modelling aspects of the SLS AM process, but principally has been applied to the manufacturing process itself, particularly the deposition of the particle layer and the sintering melt process. Various papers in the literature investigate the spreading process, particle packing, or the melting and fusion, or attempt to integrate all three areas.

Bed preparation typically involves either rollers or the use of a blade to level the bed. [26] use DEM to investigate the flow of powder layered by a blade, comparing with video recordings of the process for validation. A recent study [27] investigated the packing

 doi:10.20944/preprints202106.0688.v1

fraction and its variation with gap thickness and blade velocity for the deposition of a thin powder layer representative of a titanium alloy AM powder. [28] used DEM to model the spreading of non-spherical particles as a compact layer for sintering. They used Scanning Electron Microscopy to characterise the shapes of particles of commercial and custom-milled PEK/PEEK polymer composites, which were then represented in the DEM code (LAMMPS [29]) using composite particles built from the basic spheres. This enabled them to examine the relationship between particle shape, spreading (via roller or blade) and properties of the resulting bed.

Spreading using rollers has also been investigated using continuum mechanics methods. As discussed above, this requires the development of appropriate constitutive relations. Suitable equations have been developed [30] and applied in FE [31] and mathematically [32]. As is recognised, such methods cannot easily incorporate particle shape information in the way that DEM can, but the simulation cost is significantly lower than full DEM. We also recognise that whilst the particle shape is highly relevant for particle packing, it may be less so when the particles are fluidised, as is the case for our application. A radically different approach to the spreading is used by Desai and Higgs [33] who use back propagation Neural Networks trained on a combination of experimental and physics-based (in-house DEM) modelling of particle spreading to predict spread layer properties such as mass of material, layer roughness and porosity.

DEM can also be used to model heat transfer between particles, and so has found a use in modelling the sintering process, incorporating suitable particle/particle interactions to model the fusion [34–36]. Wei *et al* [37] review mechanistic models for metal based AM, principally concentrating on the thermal and hydrodynamic aspects of the melt pool created by the local melting, but do cover some aspects of powder packing models used to calculate aspects of the initial layering process.

In [38], Steuben *et al* present the modelling and design of an in-house DEM-based multiphysics code capable of simulating the particle deposition and sintering process for complete components; the simulation of the construction of a turbine blade is demonstrated. Performance benchmarking with the well known DEM package LIGGGHTS [39] is also presented. Lee and collaborators [40] use the LIGGGTS package to simulate the whole SLS process, with a simplified powder deposition process, recoating, laser heating and holding process. They also validate the basic DEM modelling using the experimental case of metal particles draining from a hopper.

Another area in which metal particles are being processed for AM is for direct energy deposition methods such as coaxial laser metal deposition. [41] uses the commercial CFD code CFD-ACE+ to model the gas-propelled flow of metal powder before and after leaving the nozzle. In this work, the gas flow is simulated using continuum mechanics (Finite Volume CFD) and then Lagrangian particle tracking utilised to track the particle behaviour in the gas stream. Similar methodology was used in [42] who compare with experimental data for different nozzles, and in [43].

1.4. Overview and structure of the Paper

In contrast to the work analysed in section 1.3 above, our primary interest here is in the powder removal from the interior structure of a (largely) finished AM component. Modelling this requires the computational modelling of a range of granular physics, including energisation from the wall motion during part vibration and the resulting flow of the fluidised medium. The work presented in this paper details the development of an Eulerian multiphase model for metal particles characteristic of AM use and its validation against experimental data taken from the literature. The rationale behind the choice of a continuum mechanics approach here over the more detailed DEM models was to do with relative computational cost, particularly when applied to geometrically highly complex problems; DEM is unlikely to be a practical choice for simulating powder drainage from complex components.

Preprints (www.preprints.org) | NOT PEER-REVIEWED | Posted: 29 June 2021 doi:10.20944/preprints202106.0688.v1

The structure of the paper is as follows. In the next section (section 2) we develop the mathematical equations used to model the powder flow and discuss their solution using the open source Computational Continuum Mechanics (CCM) tool OpenFOAM. Section 3 presents the details of the particular sub-models specifically developed to handle this type of granular metal powder flow, and their validation against experimental data from the literature. Section 4 presents the results of the full simulation model applied to a complex geometry representative of a true life case (based on the Morimoto duct geometry [44]). The results are reviewed and our major conclusions are presented in the Conclusions section (section 5).

2. System of Equations

2.1. Solver development

In this work, a two-fluid model of fluidised AM metal powder is developed based on the OpenFOAM Computational Fluid Dynamics (CFD) open source toolkit. Specifically this was based on the OpenFOAM solver `twoPhaseEulerFoam` which uses a continuum or Eulerian approach, in which the motion of the bed is considered as the motion of two interacting continua containing air and the powder. A frictional-kinetic theory is used in order to model the powder as a solid and gas. The Eulerian-Eulerian approach models particles and air using the following sub-models:

- Drag coefficient
- Granular viscosity (collisional, kinetic and frictional terms)
- Granular pressure (collisional and kinetic terms)
- Granular conductivity (collisional and kinetic terms)
- Radial distribution function
- Particle bulk density
- Production of granular energy by particle-particle collision
- Production and dissipation of granular energy by gas-particle slip

The drag coefficient implies that there is inter-phase momentum transfer. The rest are submodels used to synthesize the conservation equations with the kinetic theory for granular flows. As such some of them contain terms representing particle collision, kinetic and frictional behaviour. To complete the solver we have provided existing or new submodels for these physical mechanisms, and where these are new we have to validate the new modelling.

2.2. Governing Equations

In an Eulerian dispersed multiphase model we introduce the phase volume fraction α_i as the ratio of the volume of phase i in the cell V_i divided by the total volume of the cell V.

$$\alpha_i = \frac{V_i}{V} \tag{1}$$

and obviously $\Sigma_i \alpha_i = 1$. The continuity and momentum equations for the dispersed phase are given by Equations 2 and 3.

$$\frac{\partial}{\partial t}(\alpha_s \rho_s) + \nabla \cdot (\alpha_s \rho_s \vec{u}_s) = 0 \tag{2}$$

$$\frac{\partial}{\partial t}(\alpha_s \rho_s \vec{u}_s) + \nabla \cdot (\alpha_s \rho_s \vec{u}_s \vec{u}_s) = \nabla \cdot (\alpha_s \vec{\vec{\tau}}_s) - \alpha_s \nabla p - \nabla p_s + \alpha_s \rho_s \vec{g} + K_{sg}(\vec{u}_g - \vec{u}_s) \tag{3}$$

where $\vec{u}_i$, ρ_i and p_i are the velocity, density and pressure of the i-th phase ($i = s$ for the solid particulate phase and $i = g$ for the gas/continuum (air) phase). $\vec{\vec{\tau}}_i$ is the (predominantly viscous) stress, and $K_{sg}(\vec{u}_g - \vec{u}_s)$ represents the interchange of momentum between the phases due to processes such as drag. In a similar manner the conservation equations for the continuous phase are given by Equations 4 and 5.

Preprints (www.preprints.org) | NOT PEER-REVIEWED | Posted: 29 June 2021 doi:10.20944/preprints202106.0688.v1

$$\frac{\partial}{\partial t}(\alpha_g \rho_g) + \nabla \cdot (\alpha_g \rho_g \vec{u}_g) = 0 \tag{4}$$

$$\frac{\partial}{\partial t}(\alpha_g \rho_g \vec{u}_g) + \nabla \cdot (\alpha_g \rho_g \vec{u}_g \vec{u}_g) = \nabla \cdot (\alpha_g \vec{\vec{\tau}}_g) - \alpha_g \nabla p + \alpha_g \rho_g \vec{g} + K_{sg}(\vec{u}_s - \vec{u}_g) \tag{5}$$

The kinetic theory of granular flow introduces the concept of granular temperature (θ_s) to have closure with the conservation equations [45,46]. Therefore, the properties of the dispersed phase are function of this granular temperature, which is determined by solving the granular energy transport equation, given by Equation 6.

$$\frac{3}{2}\left[\frac{\partial}{\partial t}(\alpha_s \rho_s \theta_s) + \nabla \cdot (\alpha_s \rho_s \theta_s \vec{u}_s)\right] = (\nabla p_s \vec{\vec{I}} + \vec{\vec{\tau}}_s) : \nabla \vec{u}_s + \nabla \cdot (\kappa_s \nabla \theta_s) - J_{coll} - J_{vis} \tag{6}$$

2.3. Sub Models

Both the dispersed phase and the continuous phase are treated as Newtonian fluids and the stress tensors are given by Equations 7 and 8.

$$\vec{\vec{\tau}}_s = \mu_s(\nabla \vec{u}_s + \nabla \vec{u}_s^T) + (\lambda_s - \frac{2}{3}\mu_s)(\nabla \cdot \vec{u}_s)\vec{\vec{I}} \tag{7}$$

$$\vec{\vec{\tau}}_g = \mu_g(\nabla \vec{u}_g + \nabla \vec{u}_g^T) - \frac{2}{3}\mu_g(\nabla \cdot \vec{u}_g)\vec{\vec{I}} \tag{8}$$

The particle bulk density is given by Equation 9.

$$\lambda_s = \frac{4}{3}\rho_s \alpha_s^2 d_s g_0 (1 + e_s)\left(\frac{\theta_s}{\pi}\right)^{1/2} \tag{9}$$

The dissipation of granular energy by particle-particle collision is given by Equation 10.

$$J_{coll} = 3\rho_s \alpha_s^2 g_0 (1 - e_s^2)\theta_s \left(\frac{4}{d_s}\sqrt{\frac{\theta_s}{\pi}} - \nabla \cdot \vec{u}_s\right) \tag{10}$$

The production and dissipation of granular energy by gas-particle slip is given by Equation 11 from Louge.

$$J_{vis} = 3\beta\theta - \frac{\beta^2 d_s (\vec{u}_s - \vec{u}_g)^2}{4\alpha_s \rho_s (\pi\theta)^{1/2}} \tag{11}$$

Since the dispersed phase has relatively small particles and a large density, the interphase drag force dominates over the other forces such as lift and virtual mass. Therefore, the K_{sg} coefficient has just a drag contribution. The Gidaspow-Ergun-Wen-Yu drag model is suitable for both dense and dilute flows. The Ergun model is based on fixed liquid-solid beds at packed conditions ($\alpha_s > 0.2$) given by Equation 12. The Wen-Yu model is based on settling experiments of solid particles in liquid and is suitable for dilute flows ($\alpha_s < 0.2$) as shown by Equation 13.

$$K_{sg} = 150\frac{\mu_g \alpha_s^2}{d_s^2 \alpha_g^2} + 1.75\frac{\rho_g \alpha_s}{d_s \alpha_g}|\vec{u}_s - \vec{u}_g| \tag{12}$$

$$K_{sg} = \frac{3}{4}\frac{C_d \rho_g \alpha_g \alpha_s |\vec{u}_g - \vec{u}_s|}{d_s}\alpha_g^{-2.65} \tag{13}$$

The drag coefficient is given by Equation 14.

Preprints (www.preprints.org) | NOT PEER-REVIEWED | Posted: 29 June 2021 doi:10.20944/preprints202106.0688.v1

$$C_d = \begin{cases} \frac{24}{Re_s}(1 + 0.15Re_s^{0.687}) & Re_s < 1000 \\ 0.44 & Re_s \geq 1000 \end{cases} \tag{14}$$

$$Re_s = \frac{\rho_g d_s |\vec{u}_g - \vec{u}_s|}{\mu_g} \tag{15}$$

The solid stress tensor contains shear and bulk viscosities arising from particle momentum exchange due to translation and collision. A frictional component of the viscosity can also be included to account the effect of the viscous-plastic transition when the maximum solids volume fraction is reached, as shown by Equation 16.

$$\mu_s = \mu_{s,coll} + \mu_{s,kin} + \mu_{s,fric} \tag{16}$$

The kinetic viscosity model developed by Gidaspow is given by Equation 17.

$$\mu_{s,kin} = \frac{1}{6}\sqrt{\theta_s \pi}\rho_s d_s \alpha_s + \frac{10}{96}\sqrt{\theta_s \pi}\frac{\rho_s d_s}{(1+e_s)g_0} \tag{17}$$

The collisional viscosity model by Gidaspow is given by Equation 18.

$$\mu_{s,coll} = \frac{4}{5}\alpha_s^2 \rho_s d_s g_0 (1+e_s)\sqrt{\frac{\theta_s}{\pi}} + \frac{1}{15}\sqrt{\theta_s \pi}\rho_s d_s g_0 (1+e_s)\alpha_s^2 \tag{18}$$

When the solid volume fraction exceeds a critical value $\alpha_{s,min}$, the solid viscosity given by Equation 20 is added to the viscosities calculated from Equations 17 and 18 and limited beyond $\alpha_{s,max}$.

$$p_{s,fric} = \begin{cases} Fr\frac{(\alpha_s - \alpha_{s,min})^\eta}{0.05^p} & \alpha_s \geq \alpha_{s,max} \\ Fr\frac{(\alpha_s - \alpha_{s,min})^\eta}{(\alpha_{s,max} - \alpha_s)^p} & \alpha_{s,min} < \alpha_s < \alpha_{s,max} \\ 0 & \alpha_s \leq \alpha_{s,min} \end{cases} \tag{19}$$

$$\mu_{s,fric} = \frac{\sqrt{2}p_{s,fric}sin\phi_f}{2\sqrt{\vec{D}_s : \vec{D}_s}} \tag{20}$$

The conductivity model developed by Gidaspow is given by Equation 21.

$$\kappa_s = \frac{150\rho_s d_s \sqrt{\theta_s \pi}}{384 g_0 (1+e_s)}\left[1 + \frac{6}{5}g_0 \alpha_s (1+e_s)\right]^2 + 2\alpha_s^2 \rho_s d_s g_0 (1+e_s)\left(\frac{\theta_s}{\pi}\right)^{1/2} \tag{21}$$

The granular pressure, p_s is given by the Lun model, as shown in Equation 22. Physically, it refers to a pressure which is created due to the movement of particles due to shear and also due to particle-particle collisions.

$$p_s = \rho_s \alpha_s (1 + 2(1+e_s)\alpha_s g_0)\theta_s \tag{22}$$

The radial distribution function used is by Sinclair-Jackson. It is a continuous function and begins at zero and asymptotes to a maximum near the maximum volume fraction $\alpha_{s,max}$. It can be seen as a measure of the probability of inter-particle contact [47].

$$g_0 = \left[1 - \left(\frac{\alpha_s}{\alpha_{s,max}}\right)^{1/3}\right]^{-1} \tag{23}$$

3. Sub-models: development and validation

The mathematical models outlined in section 2 above are by and large generic and applicable to a range of multiphase flows. For the specific problem of powder removal flow in AM, there is a range of specific physics which has to be modelled, and for which we have

 doi:10.20944/preprints202106.0688.v1

to develop and validate specific models. In this section we explain these specific models we have developed here and how they have been validated against experimental data from the literature. This includes modelling cohesive forces relevant for Aluminium powders and the effect of wall vibration. We will discuss these aspects and the experimental validation in the following section.

3.1. Cohesive forces

There are several classifications of powder that characterise the relevant forces that need to be modelled [48]. In class A (Aeratable) powders, cohesive forces can be influential, whereas in class B (Bubbling) powders, gravity dominates over cohesive forces. Class C (Cohesive) are powders where cohesion dominates and class D (Dense) lists powders confined to large or very dense particles. The classification is determined using a sub-divided chart based on the density difference between the solid and fluid phase and the mean particle size [48]. The chart has density difference on the y-axis and mean particle size on the x-axis. In the work reported here, two powders have been selected which are relevant to additive layer manufacturing, as follows:

- Inconel 625 - $\rho_s - \rho_g = 8.5 g/cm^3$, $d_{mean} = 34.4 \mu m \rightarrow$ Geldart Type B powder (cohesive force weaker than gravity)
- AlSi10Mg - $\rho_s - \rho_g = 2.7 g/cm^3$, $d_{mean} = 42.1 \mu m \rightarrow$ Geldart Type A powder (cohesive force as important as gravity)

Experimental data is available in the form of the Hallflow test, in which the time taken for a measured mass of powder to drain from a conical hopper. Figure 1 shows the boundary conditions and geometry for the Hallflow test case. The model is axi-symmetric with a segment angle of 1 degree bound between cyclic boundaries. The inlet radius is 25.4mm, whilst the outlet radius is 10mm. The domain has a total height of 78mm, and the wall is at an angle of 30 degrees to the vertical. The orifice radius is 1.25mm and 3.2mm long. The inlet and outlet boundary conditions are atmospheric, whilst the wall boundary condition is the Johnson-Jackson condition for granular flows with a specularity coefficient of 0.25. The powder supplier has made available the test results for the two powders being examined so that it can be compared with the results of the Eulerian-Eulerian simulations. In the CFD simulation the mass flow rate can be derived from the phase fraction as follows :

$$m(t) = \rho_s \int_0^V \alpha_s dV \tag{24}$$

Preprints (www.preprints.org) | NOT PEER-REVIEWED | Posted: 29 June 2021 doi:10.20944/preprints202106.0688.v1

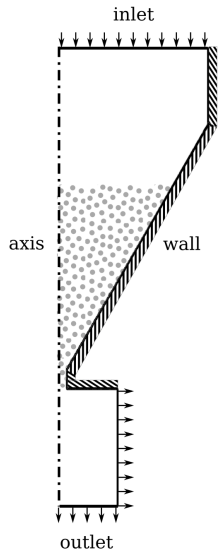

Figure 1. Basic geometry and boundary conditions for the Hallflow case (2d representation). Note that this is a conical shape hopper; the full 3d geometry is constructed from rotation around the central axis.

3.1.1. Modelling cohesive forces

Cohesive forces are weak compared to gravitational forces for the type B Inconel powder, so no cohesion model was used for this validation. Conversely, for the type A Aluminium powder, cohesive forces are important. Various cohesion models have been proposed in the literature including a model based on a cohesive pressure [49] and agglomerate diameter [50]. However the simplest model that gave sensible results used a cohesive pressure combined with a cohesive viscosity [51]. This is based on the idea of adding a pressure term to represent cohesion, as stated and validated by other researchers [49].

Cohesion is added as an additional granular pressure and viscosity. Equation 25 is the cohesive pressure and Equation 26 shows the cohesive viscosity.

$$p_c = C_0 \frac{6\sqrt{2}F_{ip}\sqrt{\theta_p}}{u_t d_p} |\nabla \alpha_p| \tag{25}$$

$$\nu_c = p_c \frac{\pi}{6(1-\alpha_p)} \tag{26}$$

C_0 in Equation 25 is a factor used due to the uncertainty about the exact value of F_{ip}, the inter-particle cohesion force. With the Aluminium powder (type A) it is assumed that van der Waals forces are the primary source of cohesion, but there is still uncertainty over the value of C_0 in the model. [52]. In order to calibrate the C_0 value, the Hallflow test is utilised with data supplied by the powder manufacturer LPW [53]. The velocity u_t is given by Equation 27

$$u_t = \sqrt{\frac{4}{3}\frac{(\rho_s - \rho_g)}{\rho_g}\frac{d_p g}{C_d}} \tag{27}$$

Preprints (www.preprints.org) | NOT PEER-REVIEWED | Posted: 29 June 2021 doi:10.20944/preprints202106.0688.v1

3.1.2. Results – Hallflow test

Since cohesive forces are weak compared to gravitational forces for the type B Inconel powder, no cohesion model was used for this validation. Figure 2.a. shows that the model predicts a linear variation in the mass over time. For the experimental data, only the initial mass and the time to empty were available [54] and so we have had to assume a constant value for the flow rate. However it is reasonable to assume this, as shown in experiments by measuring the mass over time [55]. In detail, the emptying process consists of an initial transient as the flow process starts, followed by a pseudo-steady state period when the flow is established during which the hopper empties, finishing with a final transient as the remaining powder drains away. The pseudo-steady state period represents almost all of the emptying process. The flow rate during this period is constant and it is this region that is used for measuring the mass flow rate. The difference for the time to empty for 50g of powder between the Hallflow data and the CFD model is less than 4% and the mass flow rate is less than 3% different.

With the Aluminium powder (type A) where van der Waals forces are the primary source of cohesion, we need to calibrate the value of C_0. Figure 2.b. shows that the cohesion model improves the comparison with the Hallflow data, but that the choice of the factor C_0 needs to be optimised to produce the correct mass flow rate. The time to empty is within 2% of the Hallflow test using a cohesion factor of 7.5. It is clear from Figure 4 that the cohesion model has a significant influence on the solid volume fraction, due to the addition of the cohesive pressure and viscosity. However, it is unlikely that this cohesion model can be used in case of vibrating walls, as the breakup of agglomerates by the dominance of vibrational energy over collisional and cohesive energy is not being considered. For this reason the model is limited to Hallflow data where vibration is not being used to fluidize the powder.

3.2. Wall Vibration

In order to simulate wall normal vibration, it was necessary to develop a new boundary condition. Several approaches were considered, including a sinusoidal gravity term [56], mesh motion, finite element coupling and use of the granular temperature [57]. The frequency of vibration (on the order of 10 kHz) is likely to be far too high to utilise mesh motion and finite element coupling, due to the computational overhead of simulating the individual wall motions involved. On the other hand, a sinusoidal gravity term is simplest, but only allows for vibration to be applied in the direction of the gravity vector. The reality of the vibration applied to remove the powder is that it is wall-normal. Therefore the most efficient method, which also provided physical realism, was to utilise the fact that the kinetic theory of granular flows requires a pseudo-heat flux at the wall, which can be used to simulate wall-normal vibration. The equation for wall vibration was developed by Richman [57], by considering that random vibrations occur in all three perpendicular directions. Here it is assumed that in-plane vibration components do not contribute to the energy transfer such that only wall-normal vibration is considered. The form used here was given by Viswanathan [58].

$$\vec{n} \cdot \vec{q} = \frac{\pi\sqrt{3}}{6\alpha_{max}} \phi \rho_p \alpha g_0 \theta^{1/2} \vec{u}_{sl}^2 + Q_0 \tag{28}$$

$$Q_0 = \left(\frac{2}{\pi}\right)^{1/2} 4\rho\alpha g_0 \left[V_{rms}^2 (\theta + V_{rms}^2)^{1/2}\right] \tag{29}$$

$$V_{rms} = \frac{a\omega}{\sqrt{2}} \tag{30}$$

For comparison purposes, the validation case also includes a model using a gravity term representing the vibration. The equation for this simply modifies the global body force of gravity in the momentum equation for the air and particle phases [56].

Preprints (www.preprints.org) | NOT PEER-REVIEWED | Posted: 29 June 2021 doi:10.20944/preprints202106.0688.v1

a.

b.

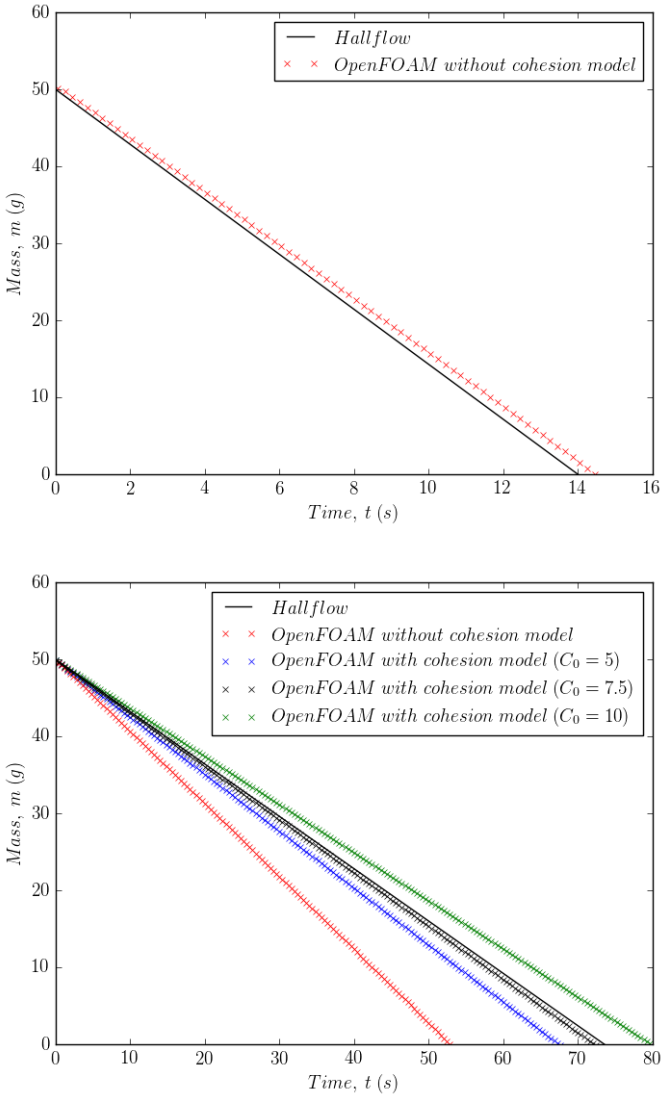

Figure 2. Comparison between the Eulerian-Eulerian model and the Hallflow experimental data. a. Results for Inconel (Geldart Type B) without cohesive force model. b. Results for Aluminium powder (Geldart Type A) with different values of C_0.

$$\vec{a} = \vec{g}(1 - a\omega^2 sin(\omega t)) \tag{31}$$

3.2.1. Wall Normal Vibration Test Case

Validation of the vibration modelling was carried out using a vibrofluidisation case for which experimental data (using large dolomite and fine glass particles) are available [59]. Figure 3 shows the boundary conditions for the two models analysed in this section. The domain is 2D with a width and height of 400mm, and a depth of 5mm. The domain is initially filled with particles to a height of 20mm or 30mm depending on the test case. The boundary condition at the outlet is an atmospheric pressure boundary. The wall boundaries can either be fixed or vibrating. If fixed, then a sinusoidal gravity vector is imposed in the vertical plane. If vibrating, the frequency can vary between 20.1Hz and 37.1Hz according to the validation case data, whilst the amplitude is fixed at 1.25mm.

Preprints (www.preprints.org) | NOT PEER-REVIEWED | Posted: 29 June 2021 doi:10.20944/preprints202106.0688.v1

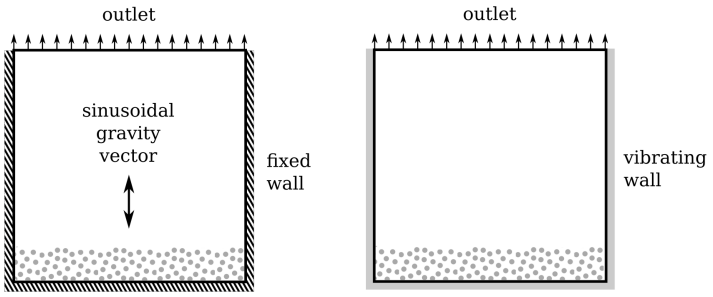

(a) With sinusoidally varying gravity body force

(b) With pseudo-heat flux boundary on granular temperature.

Figure 3. Square geometry used to validate the vibration modelling.

3.2.2. Effect of Vibration on Solid Volume Fraction Field

Figure 4 shows the volume fraction field as computed by considering that the wall boundary condition is given by the pseudo-heat flux in Equation 28. It is clear that increasing the frequency of vibration dilutes the volume fraction field and increases the height of the splashes seen near the corners.

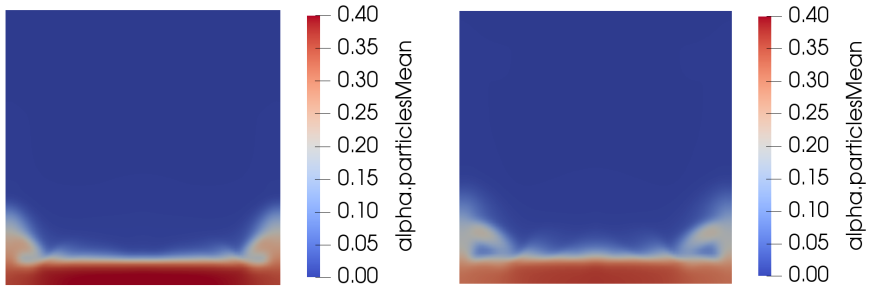

(a) f=20.1Hz

(b) f=26.1Hz

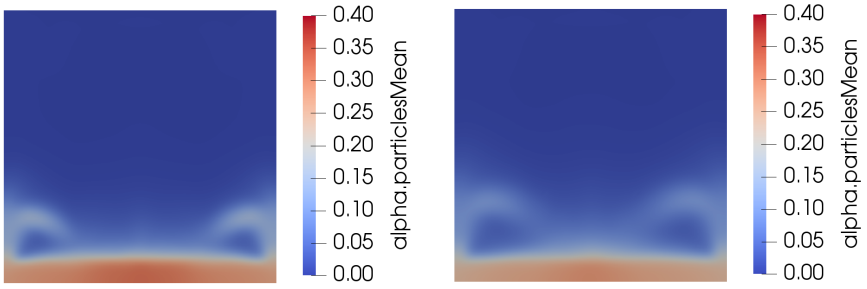

(c) f=32.1Hz

(d) f=37.1Hz

Figure 4. Effect of frequency on solid volume fraction field.

Figure 5 compares the result of assuming the gravity body force can represent vibration using Equation 31 with Equation 28 using the pseudo-heat flux approach. The gravity body force approach cannot capture the splashes seen at the corners, because vibration is only implemented in the vertical direction of gravity.

3.2.3. Effect of Vibration on Surface Height

Quantitative validation of the new boundary conditions was sought using the height of the volume fraction field as an isosurface at a value of 0.1. These measurements are shown in Figure 6 via a comparison between experimental measurements [59], the pseudo-heat flux approach of Equation 28 and the gravity body force approach of Equation 31. The results show that the difference is less than 10% and the trend is broadly similar.

Preprints (www.preprints.org) | NOT PEER-REVIEWED | Posted: 29 June 2021 doi:10.20944/preprints202106.0688.v1

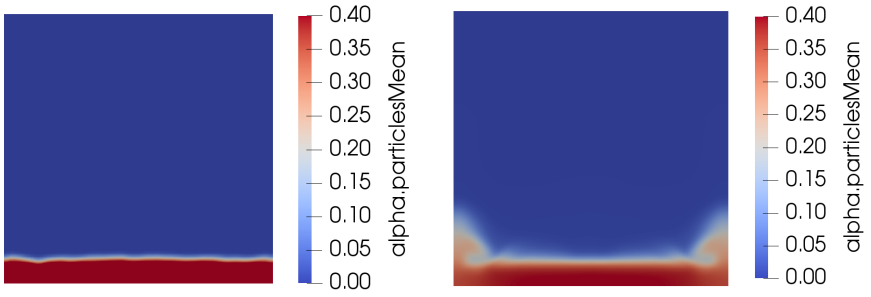

(a) With gravity body force **(b)** With wall normal heat flux

Figure 5. Different modelling techniques for vibration.

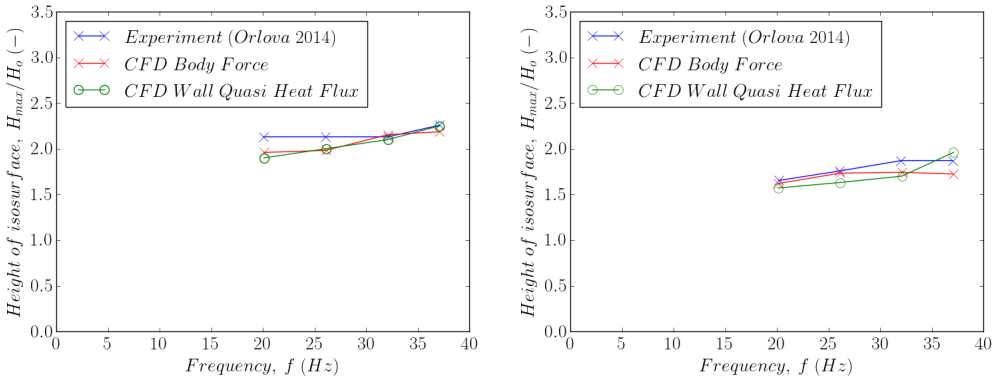

(a) $H_0 = 20mm$ **(b)** $H_0 = 30mm$

Figure 6. Validation of wall normal vibration model.

3.2.4. Effect on granular temperature

The previous friction model (equation 20) applied to a case where wall-normal vibration was not used. In cases where the particles are relatively large (1.75mm) and the vibrational frequency is low (<40Hz), as in the experiments used above, this is still a reasonable assumption [56]. For cases where $d \to 0$ and higher frequency vibration, the vibration may well affect the frictional viscosity. To account for these cases, the model of Srivastava-Sunderesan is used. This was verified by comparison with the test case of Srivastava-Sunderesan (which differs by its use of alternative submodels). This differs from the usual form of the Schaeffer frictional stress, as it includes a term that allows strain rate fluctuations (represented by granular temperature) θ/d^2.

$$\mu_f = \frac{\sqrt{2} p_f sin\phi}{\sqrt{\vec{\vec{D}} : \vec{\vec{D}} + \theta/d^2}} \tag{32}$$

$$\mu_f = \frac{\sqrt{2} p_f sin\phi}{\sqrt{\vec{\vec{D}} : \vec{\vec{D}}}} \tag{33}$$

4. Modelling of a complex duct

The objective of the work reported in this paper is to provide a model for the powder drainage from arbitrarily complex internal ducting manufactured through AM. Having developed such a model and validated the main new models (section 3) we are now in a position to apply this to a more complex geometry. The geometry used for this is derived from the geometry proposed by Morimoto [44,60], developed as an optimal shape design for a recuperator heat exchanger. The design uses oblique wavy walls to optimise heat exchange between separated flows of hot and cold fluid, and has been designed for use in

Preprints (www.preprints.org) | NOT PEER-REVIEWED | Posted: 29 June 2021 doi:10.20944/preprints202106.0688.v1

compact heat exchangers. As such this is characteristic of the types of AM components we are interested in [61].

4.1. Test Case Description

Figure 7 shows the boundary conditions for the Morimoto test case. The duct has three wavelengths with an amplitude of 0.25mm and wavelength of 2.5mm with a wall separation of 1mm in both orthogonal directions. This duct was fed from a square-cornered hopper. The reason for this was to make the mass versus time profile non-linear by allowing powder to become trapped in the corners. This also provided the opportunity to investigate the effect of further manipulation of the unit, in particular the effect of tilting the unit to remove powder from the corners.The hopper has a width and depth of 10mm, with a height of 7.5mm, the outlet has a width and depth of 10mm and a height of 5mm. The hopper is initially filled with a mass of powder of 2g, a value chosen to minimise the time required to empty the vessel whilst still allowing linear and non-linear regions of the flow regime to be observed. The inlet and outlet boundary conditions are set to atmospheric pressure.

In each of the following cases the effects of manipulation, vibration and the effect of both together are studied. The effect of unit manipulation is simulated by allowing the direction of the gravity vector to precess around a cone of half angle θ (θ ranging from 0° to 20°) by defining it as

$$\vec{g} = (g_x, g_y, g_z) \tag{34}$$

$$g_x = 9.81 \sin\theta \sin(\omega t) \tag{35}$$

$$g_y = -9.81 \cos\theta \tag{36}$$

$$g_z = 9.81 \sin\theta \cos(\omega t) \tag{37}$$

with a rotational speed ω. This appears as an additional body force in the momentum equation for both the particle phase and the air phase. It also introduces a centrifugal acceleration of form

$$\vec{C} = -\rho(\vec{\omega} \times (\vec{\omega} \times \vec{r})) \tag{38}$$

This appears as a source term on the right hand side of the momentum equation for the particle phase [62]. It is assumed that the air phase is unaffected by centrifugal forces due to its relatively low density. The effect of vibration is introduced by use of the pseudo-heat flux given by Equation 28, which is introduced as a new boundary condition into the code. The vibrating walls use this pseudo-heat flux condition with a frequency of 20Hz and an amplitude of 1.25mm and a specularity coefficient of 1 unless otherwise specified. It was found that application of the wall normal vibration to all walls resulted in powder being driven against gravity in the hopper. This meant that it could no longer supply the Morimoto geometry with powder. Instead, the vibration was applied only to the Morimoto section as shown in Figure 7. The fixed walls use the Johnson-Jackson boundary conditions for partial slip with a specularity coefficient of 0.25. Equation 24 was used to measure the mass flow over time.

In all, four different wall separations were investigated; 0.5mm, 1mm, 1.5mm and 2mm. The CPU time for this geometry varied with the wall separation from 21h 44m for 0.5mm to 2h 14m for 2mm. This is largely due to the time taken to empty the device, as the number of cells varied from 63,756 for 0.5mm to 150,108 for 2mm, whilst the time to empty varied from 55.0 seconds for 0.5mm to 2.8 seconds for 2mm. This was measured on a 12 processor run, on Intel Xeon processors at 2.00GHz, with 35MB cache.

Preprints (www.preprints.org) | NOT PEER-REVIEWED | Posted: 29 June 2021 doi:10.20944/preprints202106.0688.v1

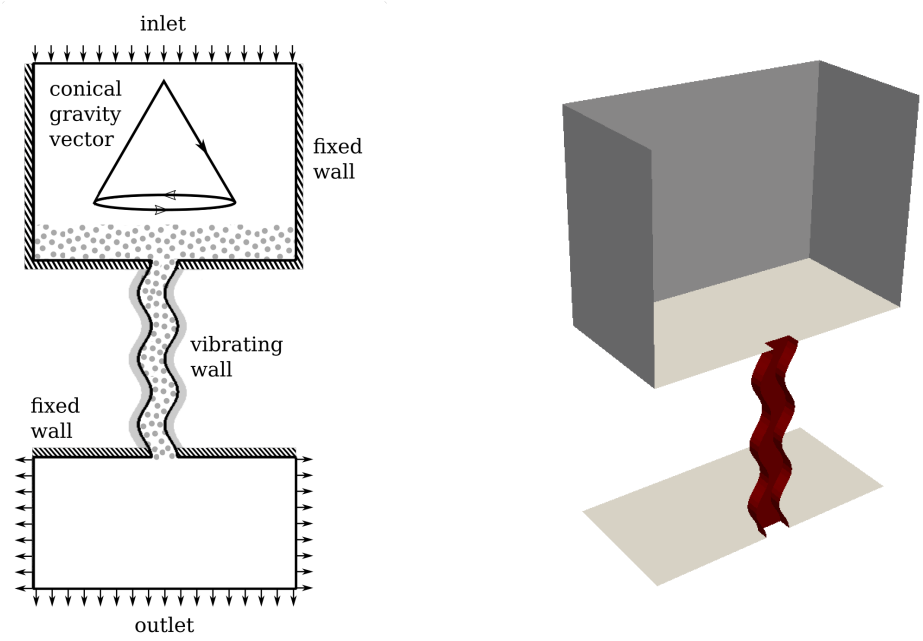

Figure 7. Morimoto geometry and boundary conditions (half of the domain is shown). The section in red is set as a vibrating wall.

4.2. Effect of Manipulation/Vibration

The effect of manipulation (moving the unit bodily around) with or without wall vibration (i.e. shaking the unit) is examined in this section. The basic effect of the manipulation is shown in Figure 8 which contrasts the powder remaining in the hopper at t=8s (i.e. almost empty) for a stationary geometry (Figure 8a) with that for a rotational manipulation $\theta = 10°$, $\omega = 0.1 rad/s$. As can be seen, the tilting manipulation has clearly encouraged more of the powder to drain out of the unit which would otherwise become trapped in the corners of the hopper. Figure 9 demonstrates the drainage of the powder over time for various wall separation. The effect of the corners of the square hopper is to slow the powder emptying in the final stages (solid lines for the different duct geometries), whilst the manipuation sequence clearly reduces this effect (dashed lines).

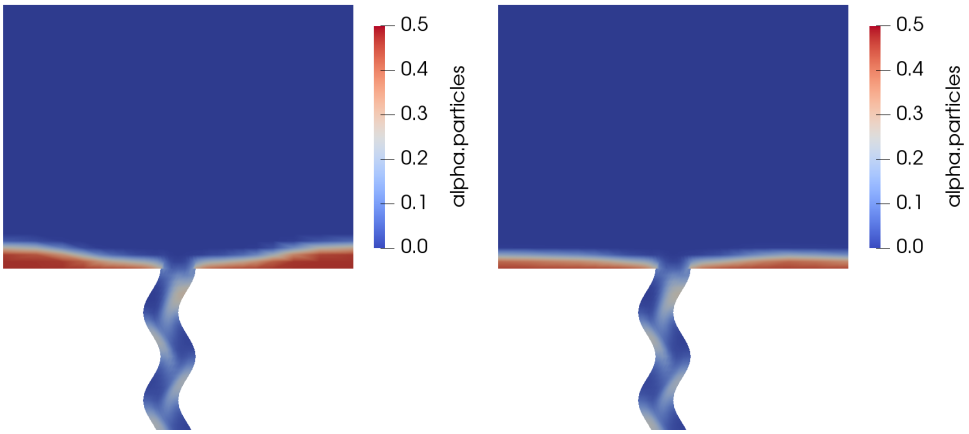

(a) $W = 1mm$ at t=8s, no vibration, no manipulation.

(b) $W = 1mm$ at t=8s, no vibration, $\theta = 10deg$, $\omega = 0.1 rad/s$.

Figure 8. Effect of manipulation sequence on the volume fraction field.

We can contrast this with Figures 10 and 11 which show the combined effect of manipulation and vibration on the emptying. Figure 10 shows that the combination influences the final transient of the emptying process. This suggests that the best combination is to use the

Preprints (www.preprints.org) | NOT PEER-REVIEWED | Posted: 29 June 2021 doi:10.20944/preprints202106.0688.v1

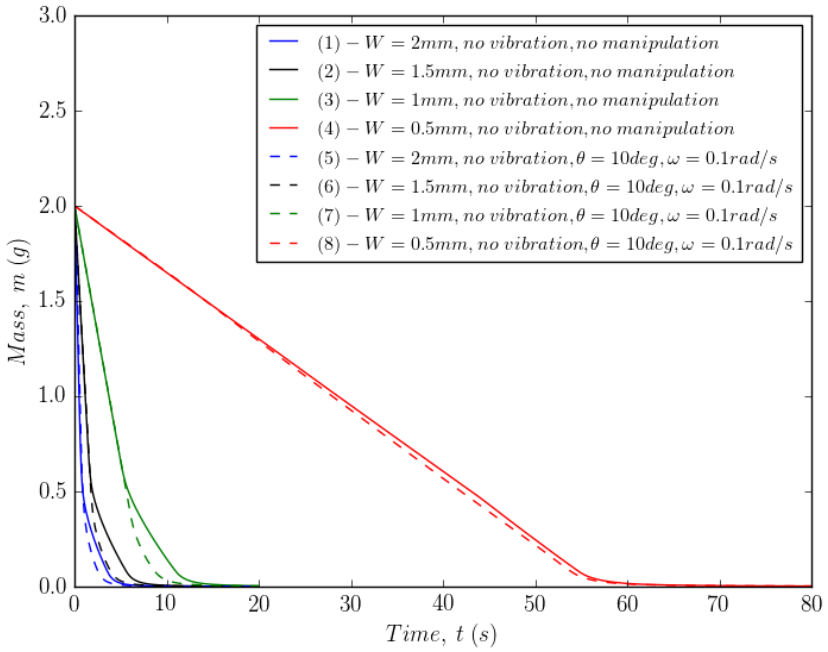

Figure 9. Effect of manipulation sequence.

energisation of wall normal vibration together with manipulation. Figure 11 demonstrates that the manipulation sequence with vibration has a similar effect to that shown in Figure 8, since powder can be more effectively removed from the corners with manipulation. This feeds the subsequent energisation of the powder by vibration in the Morimoto section.

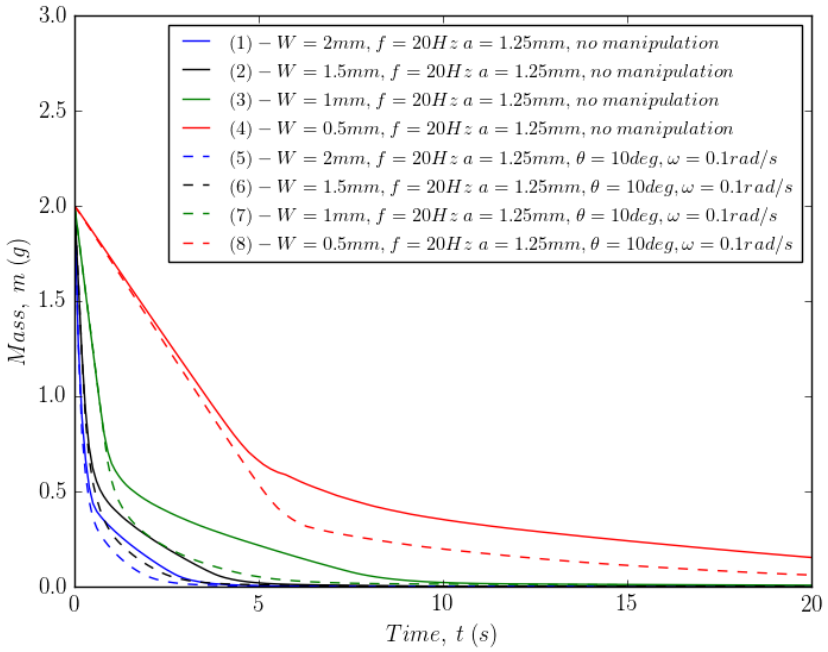

Figure 10. Effect of manipulation and wall normal vibration.

Two measures were used in order to quantify the previous figures, the maximum mass flow and the time to empty. The maximum mass flow was taken during the pseudo-steady state region ($t = t_0$) by taking the steady gradient of the mass versus time profile as shown in Equation 39. The time to empty was taken when the mass fell to 1% of the original mass ($m_1 > 0.02g$ and $m_2 < 0.02g$) and was determined using linear interpolation as shown in Equation 40.

Preprints (www.preprints.org) | NOT PEER-REVIEWED | Posted: 29 June 2021 doi:10.20944/preprints202106.0688.v1

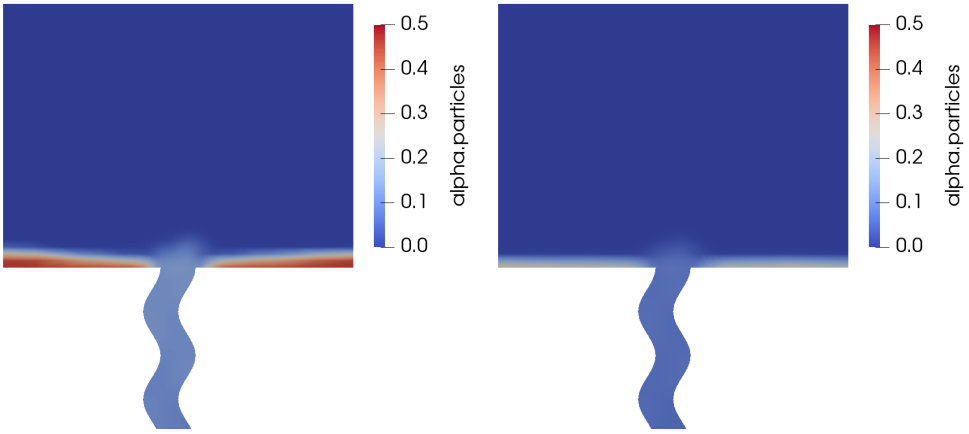

(a) $W = 1mm$ at t=5s, $f = 20Hz, a = 1.25mm$, no manipulation.

(b) $W = 1mm$ at t=5s, $f = 20Hz, a = 1.25mm$, $\theta = 10deg, \omega = 0.1rad/s$.

Figure 11. Effect of manipulation sequence and vibration on the volume fraction field.

$$\dot{m}_{max} = \left.\frac{\partial m}{\partial t}\right|_{t=t_0} \tag{39}$$

$$t_{empty} = t_1 + \frac{t_2 - t_1}{m_2 - m_1}(0.02 - m_1) \tag{40}$$

Figure 12 shows the maximum mass flow, $\dot{m}_{max}$, versus frequency, f, for two wall separations 1mm and 0.5mm. Equation 41 was used to fit the data. The fit suggests that the maximum mass flow tends to reach a limit at high frequency.

$$\dot{m}_{max} = a(f^b)exp\left(-\frac{c}{f}\right) \tag{41}$$

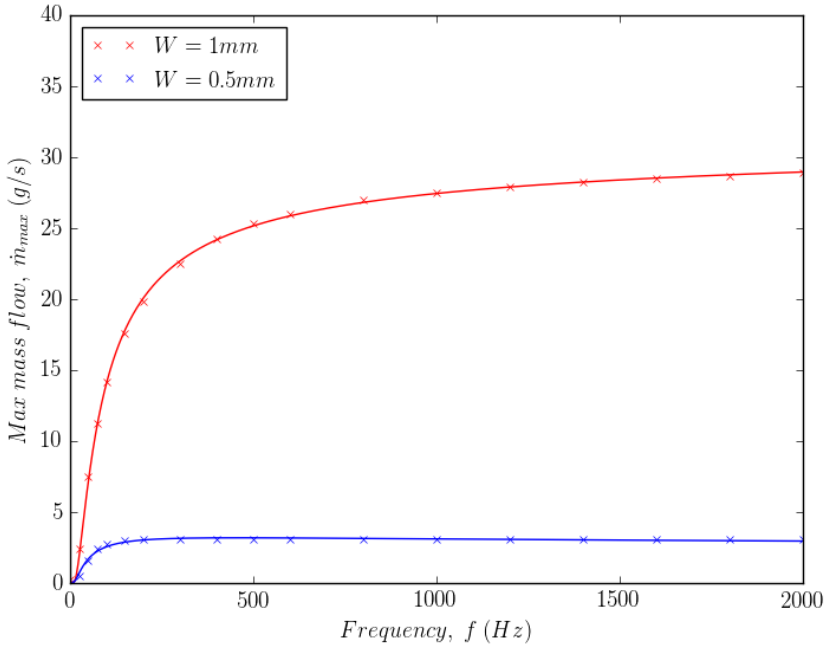

Figure 12. Maximum mass flow versus frequency at high frequencies.

Preprints (www.preprints.org) | NOT PEER-REVIEWED | Posted: 29 June 2021 doi:10.20944/preprints202106.0688.v1

At high frequencies, the model behaves as expected, reaching a limit to the maximum mass flow. This limit is clearly larger for larger wall separations, as has been reported in the literature [63]. At low frequencies, Figure 13 shows that the continuum model shows a continuous reduction in the maximum mass flow. This is contrary to the sudden reduction shown in the literature for cohesive aluminium powder [63], however no results are available for non-cohesive Inconel powder. Nevertheless, these results may only be valid for type B powders such as unused Inconel 625. With cohesive type A powders, where the initial condition might include particle agglomeration, it is expected that a model of agglomeration and breakup would be required.

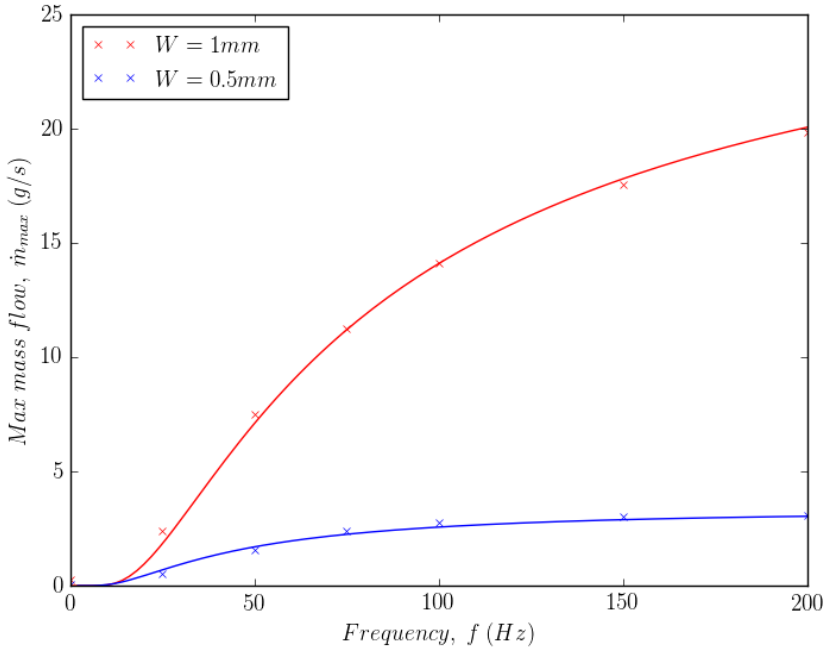

Figure 13. Maximum mass flow versus frequency at low frequencies.

Figure 14 shows the time to empty plotted against the conical angle of gravity for two different rotational speeds 0.1 rad/s and 1 rad/s. For both speeds, it appears that a minimum time to empty is observed between an angle of 5° and 10°. This is because at 0°, without an angle of gravity, powder is trapped in both corners of the device. At around 7.5°, the angle is sufficiently large to empty the corners more quickly, whilst a larger angle such as 20° traps powder in one corner more severely. Figure 15 plots the time to empty against the rotational speed of the gravity vector for two angles, 0° and 10°. For both angles it is clear that for rotational speeds of the order of 0.1 rad/s, the emptying process is dominated by gravity, as the centrifugal acceleration is too small to have an influence. However, at higher rotational speeds the centrifugal acceleration increases the time to empty by sending particles away from the emptying orifice, as shown by Figure 16. Although it appears as though centrifugal forces are detrimental to powder removal, with a change in orientation, it may be possible to use them to empty powder from the device. In any case, more complex geometries are required in order to ascertain whether the manipulation sequence depends on the specific geometry in question.

5. Conclusions

Post-processing of an AM-manufactured component is a key element of the manufacturing chain of AM, and can make a substantial difference to the physical behaviour of the component. With metal powder-based techniques such as SLS, one key aspect here is the removal of surplus powder from the internal structure of the component, where it might well affect the successful operation of that component (eg by blocking flow of fluid in a

Preprints (www.preprints.org) | NOT PEER-REVIEWED | Posted: 29 June 2021 doi:10.20944/preprints202106.0688.v1

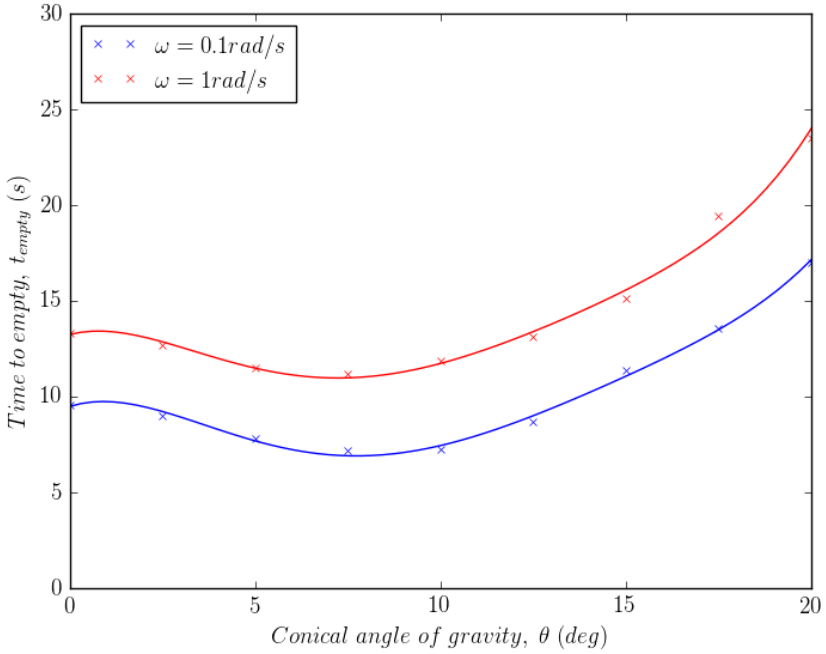

Figure 14. Time to empty versus angle of gravity vector.

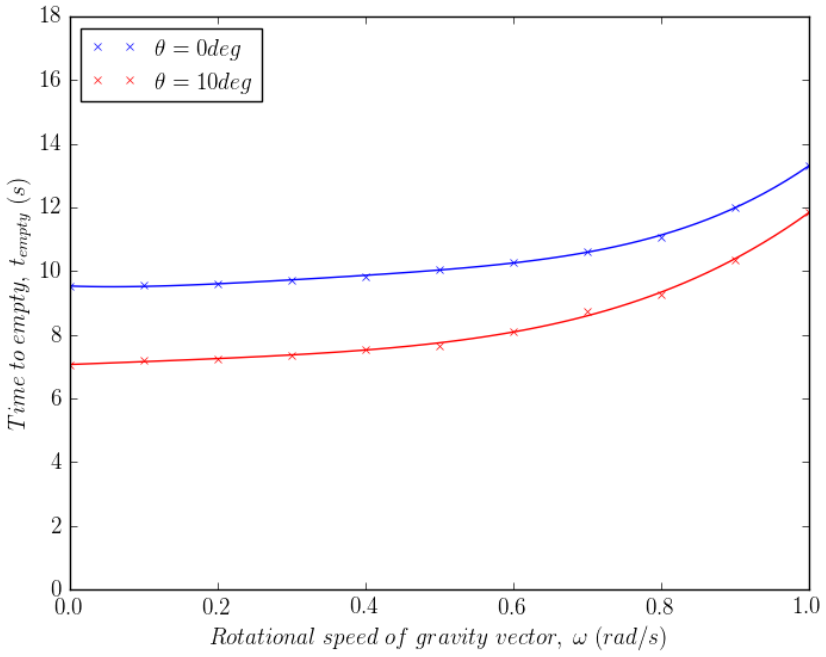

Figure 15. Time to empty versus rotational speed of gravity vector.

heat exchanger). This is typically achieved through vibrational fluidisation of the packed powder, allowing it to drain out of the component.

In this paper we present a continuum model of the powder flow developed specifically to model this process. The individual models for aspects such as cohesion and vibration have been successfully validated against data from both the academic literature and against standard test cases. In particular experimental data for the Hall flow test was used to validate the model of powder flow for Inconel and aluminium. The model of the wall vibration using a pseduo-heat flux boundary condition was also validated against experimental data from the literature. The limitations of these validations were that they dealt with un-used powder and also dealt with simple geometries that treated the

Preprints (www.preprints.org) | NOT PEER-REVIEWED | Posted: 29 June 2021 doi:10.20944/preprints202106.0688.v1

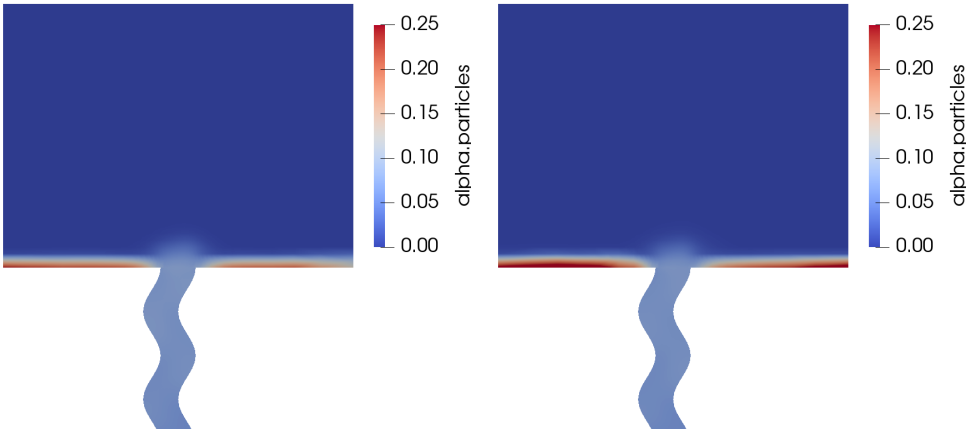

(a) $W = 1mm$ at t=5s, $f = 20Hz, a = 1.25mm$, $\theta = 10deg, \omega = 0.1rad/s$.

(b) $W = 1mm$ at t=5s, $f = 20Hz, a = 1.25mm$, $\theta = 10deg, \omega = 1rad/s$.

Figure 16. Effect of the rotational speed of the gravity vector on the volume fraction field.

wall vibration as a fixed frequency and amplitude across the whole of the geometry. Nevertheless, additional submodels were proposed including a friction model that allowed strain-rate fluctuations, a conical gravity vector and a term for centrifugal acceleration.

A more complex test case was then developed based on a geometry proposed [60] for heat exchanger applications with the purpose of developing strategies for the manipulation sequence and energisation through wall-normal vibration. Several different wall separations for this wavy duct were investigated. The case also included sharp corners in the powder hopper in order to test out the manipulation sequence. To provide effective energisation, wall normal vibration was provided in areas where the powder flow was restricted. This allowed powder feed to be controlled by the manipulation sequence and powder flow by the energisation. The manipulation sequence was found to be effective at removing powder trapped in the corners at the end of the emptying process, whilst the energisation dictated the maximum mass flow in the pseudo-steady region.

Trends in the maximum mass flow and time to empty revealed that a no-flow wall separation existed. In addition, the manipulation sequence had no influence on the maximum mass flow, which is instead directly determined by the magnitude of the RMS velocity of the wall normal vibration. The time to empty was roughly equally affected by wall normal vibration and by manipulation, however the most effective strategy to minimise the time to empty was to combine wall normal vibration with the manipulation sequence. Analysing the influence of vibration frequency on the maximum mass flow showed that the mass flow reaches a plateaux at high frequency as expected from the literature. However, the behaviour at low frequencies remains unvalidated. It was suggested that a diameter model could be used to introduced frequency dependent particle breakage for agglomerates in the case of a more cohesive powder. The time to empty was influenced by both the angle of the gravity vector and the rotational frequency. It was found that an optimum conical angle of gravity existed, whilst the influence of the rotational frequency of the manupiluation sequence tended to increase the time to empty. Further studies on this with more complex geometries might reveal different optimum sequences.

In these simulations, the RMS velocity has been assumed to be constant. This may be true for a very simple component, but over a complex component, the amplitude and frequency of the solid part is likely to vary. At the very least there may be a phase shift and amplitude shift between the solid part and the powder [64]. In addition, this modelling approach does not address any stresses present in the solid structure that may limit the frequencies that can be used. Coupling with a finite element model may provide such information. The CFD model requires the input of RMS velocity, which could be obtained

from the RMS displacements of the FEA model. The FEA model would require the input of the time-varying mass of the powder, which could be obtained from the CFD model.

Author Contributions: Conceptualization, G.T. R.K. and D.B.; methodology, G.T., R.K. and A.R.; model development and validation, A.R.; analysis, A.R.; writing—original draft preparation, A.R. and G.T.; writing—review and editing, G.T.; supervision, G.T.; project administration, G.T. and D.B.; funding acquisition, G.T. and D.B. All authors have read and agreed to the published version of the manuscript.

Funding: "This research was funded by InnovateUK and EPSRC under grant EP/P030785/1 "TACDAM; Tailorable and Adaptive Connected Digital Additive Manufacturing"

Data Availability Statement: No data for public archival is reported in this study. The study does not report any data of this kind.

Conflicts of Interest: The authors declare no conflict of interest.

Abbreviations

The following abbreviations are used in this manuscript:

AM	Additive Manufacture
CFD	Computational Fluid Dynamics
DEM	Discrete Element Model
FE	Finite Element
FEA	Finite Element Analysis
FV	Finite Volume
MDM	Molecular Dynamics Model
SLS	Selective Laser Sintering

References

1. Frazier, W.E. Metal additive manufacturing: A review. *Journal of Materials Engineering and Performance* **2014**, *23*, 1917–1928. doi:10.1007/s11665-014-0958-z.
2. Renishaw Plc.. Investigating the effects of multiple re-use of Ti6Al4V powder in additive manufacturing (AM), 2016.
3. Vayre, B.; Vignat, F.; Villeneuve, F. Identification on some design key parameters for additive manufacturing: Application on Electron Beam Melting. *Procedia CIRP* **2013**, *7*, 264–269. doi:10.1016/j.procir.2013.05.045.
4. Dalquist, S.; Gutowski, T. Life Cycle Analysis of Conventional Manufacturing Techniques: Sand Casting. *Manufacturing Engineering and Materials Handling Engineering* **2004**, *2004*, 631–641. doi:10.1115/IMECE2004-62599.
5. M.B. Associates, U. Best Practice Guide For Foundry Sector Of India. *Bureau of Energy Efficiency (BEE) and Institute for Industrial Productivity (IIP)* **2012**.
6. Duru, P.; Nicolas, M.; Hinch, J.; Guazzelli, E. Constitutive laws in liquid-fluidized beds. *J.Fluid Mech* **2002**, *452*, 371 – 404.
7. Guo, Y.; Curtis, J.S. Discrete Element Method Simulations for Complex Granular Flows. *Annual Review of Fluid Mechanics, Vol 47* **2015**, *47*, 21–46. doi:10.1146/annurev-fluid-010814-014644.
8. Goldhirsch, I. Rapid granular flows. *Ann.Rev.Fluid Mech* **2003**, *35*, 267 – 293.
9. Bagnold, R.A. Experiments on a Gravity-Free Dispersion of Large Solid Spheres in a Newtonian Fluid under Shear. *Proceedings of the Royal Society of London. Series A, Mathematical and Physical Sciences* **1954**, *225*, 49–63. doi:10.1098/rspa.1954.0186.
10. Campbell, C.S. Granular material flows - An overview. *Powder Technology* **2006**, *162*, 208–229, [arXiv:cond-mat/0108517]. doi:10.1016/j.powtec.2005.12.008.
11. Aranson, I.S.; Tsimring, L.S. Patterns and collective behavior in granular media: Theoretical concepts. *Reviews of Modern Physics* **2006**, *78*, 641–692, [arXiv:cond-mat/0507419]. doi:10.1103/RevModPhys.78.641.
12. Michopoulos, J.G.; Iliopoulos, A.P.; Steuben, J.C.; Birnbaum, A.J.; Lambrakos, S.G. On the multiphysics modeling challenges for metal additive manufacturing processes. *Additive Manufacturing* **2018**, *22*, 784 – 799.
13. D.Drikakis.; Frank, M.; Tabor, G. Multiscale Computational Fluid Dynamics. *Energies* **2019**, *12*, 3272.
14. Radjai, F.; Roux, J.N.; Daouadji, A. Modeling Granular Materials: Century-Long Research across Scales. *J. Eng. Mech.* **2017**, *143*, 04017002. doi:10.1061/(ASCE)EM.1943-7889.0001196.
15. Aranson, I. *Granular Patterns*; Oxford University Press, 2009.
16. Durst, F.; Milojevic, F.; Schönung, B. Eulerian and lagrangian predicitons of particulate two-phase flows: a numerical study. *Applied Mathematical Modelling* **1984**, *8*, 101–115.
17. Da Cruz, F.; Emam, S.; Prochnow, M.; Roux, J.N.; Chevoir, F. Rheophysics of dense granular materials: Discrete simulation of plane shear flows. *Physical Review E - Statistical, Nonlinear, and Soft Matter Physics* **2005**, *72*, 1–17, [arXiv:cond-mat/0503682]. doi:10.1103/PhysRevE.72.021309.

18. Rognon, P.G.; Roux, J.N.; Naaïm, M.; Chevoir, F. Dense flows of cohesive granular materials. *Journal of Fluid Mechanics* **2008**, *596*, 21–47. doi:10.1017/S0022112007009329.
19. Jop, P.; Forterre, Y.; Pouliquen, O. A constitutive law for dense granular flows. *Nature* **2006**, *441*, 727–730. doi:10.1038/nature04801.
20. Passalacqua, A.; Fox, R.O. Implementation of an iterative solution procedure for multi-fluid gas-particle flow models on unstructured grids. *Powder Technology* **2011**, *213*, 174–187. doi:10.1016/j.powtec.2011.07.030.
21. Srivastava, A.; Sundaresan, S. Analysis of a frictional-kinetic model for gas-particle flow. *Powder Technology* **2003**, *129*, 72–85. doi:10.1016/S0032-5910(02)00132-8.
22. Zheng, Q.; Yu, A. Finite element investigation of the flow and stress patterns in conical hopper during discharge. *Chemical Engineering Science* **2015**, *129*, 49 – 57. doi:https://doi.org/10.1016/j.ces.2015.02.022.
23. Liu, S.; Zhou, Z.; Zou, R.; Pinson, D.; Yu, A. Flow characteristics and discharge rate of ellipsoidal particles in a flat bottom hopper. *Powder Technology* **2014**, *253*, 70 – 79. doi:https://doi.org/10.1016/j.powtec.2013.11.001.
24. Bharadwaj, R.; Khambekar, J.; Orlando, A.; Gao, Z.; Shen, H.; Helenbrook, B.; Royal, T.A.; Weitzman, P. A Comparison of Discrete Element Modeling, Finite Element Analysis, and Physical Experiment of Granular Material Systems in a Direct Shear Cell. *AIP Conference Proceedings* **2008**, *969*, 221–228, [https://aip.scitation.org/doi/pdf/10.1063/1.2844971]. doi:10.1063/1.2844971.
25. Liu, Y.; Gonzalez, M.; Wassgren, C. Modeling granular material blending in a rotating drum using a finite element method and advection-diffusion equation multiscale model. *AIChE Journal* **2018**, *64*, 3277–3292, [https://aiche.onlinelibrary.wiley.com/doi/pdf/10.1002 doi:https://doi.org/10.1002/aic.16179.
26. Chen, H.; Wei, Q.; Wen, S.; Li, Z.; Shi, Y. Flow behavior of powder particles in layering process of selective laser melting: Numerical modeling and experimental verification based on discrete element method. *Int.J. Machine Tools and Manufacture* **2017**, *123*, 146 – 159.
27. Fouda, Y.M.; Bayly, A.E. A DEM study of powder spreading in additive layer manufacturing. *Granular Matter* **2020**, *22*, 10.
28. Haeri, S.; Wang, Y.; Ghita, O.; Sun, J. Discrete element simulation and experimental study of powder spreading process in additive manufacturing. *Powder Technology* **2016**, *306*, 45 – 54.
29. Plimpton, S. Fast parallel algorithms for short-range molecular dynamics. *J.Comp.Phys.* **1995**, *117*, 1 – 19.
30. Johanson, J.R. A Rolling Theory for Granular Solids. *Journal of Applied Mechanics* **1965**, *32*, 842–848, [https://asmedigitalcollection.asme.org/ pdf/32/4/842/5447239/842_1.pdf]. doi:10.1115/1.3627325.
31. Dec, R.T.; Zavaliangos, A.; Cunningham, J.C. Comparison of various modeling methods for analysis of powder compaction in roller press. *Powder Technology* **2003**, *130*, 265 – 271. doi:https://doi.org/10.1016/S0032-5910(02)00203-6.
32. Shanjani, Y.; Toyserkani, E. Material spreading and compaction in powder-based solid freeform fabrication methods: Mathematical modeling. 2008, pp. 399–410.
33. Desai, P.S.; Higgs, C.F. Spreading Process Maps for Powder-Bed Additive Manufacturing Derived from Physics Model-Based Machine Learning. *Metals* **2019**, *9*, 1176.
34. Martin, S.; Guessasma, M.; Léchelle, J.; Fortin, J.; Saleh, K.; Adenot, F. Simulation of sintering using a Non Smooth Discrete Element Method. Application to the study of rearrangement. *Computational Materials Science* **2014**, *84*, 31 – 39.
35. Martin, S.; Parekh, R.; Guessasma, M.; Léchelle, J.; Fortin, J.; Saleh, K. Study of the sintering kinetics of bimodal powders. A parametric DEM study. *Powder Technology* **2015**, *270*, 637 – 645.
36. Xin, H.; Sun, W.; Fish, J. Discrete element simulations of powder-bed sintering-based additive manufacturing. *Int.J. Mechanical Sciences* **2018**, *149*, 373 – 392.
37. Wei, H.; Mukherjee, T.; Zhang, W.; Zuback, J.; Knapp, G.; De, A.; DebRoy, T. Mechanistic models for additive manufacturing of metallic components. *Progress in Materials Science* **2021**, *116*, 100703.
38. Steuben, J.C.; Iliopoulos, A.P.; Michopoulos, J.G. On Multiphysics Discrete Element Modeling of Powder-Based Additive Manufacturing Processes. Proceedings of the ASME 2016 International Design Engineering Technical Conferences & Computers and Information in Engineering Conference, IDETC/CIE, 2016.
39. Kloss, C.; Goniva, C.; Hager, A.; Amberger, S.; Pirker, S. Models, algorithms and validation for opensource DEM and CFD-DEM. *Progress in Computational Fluid Dynamics, an Int. J.* **2012**, *12*, 140 – 152.
40. Lee, W.H.; Zhang, Y.; Zhang, J. Discrete element modeling of powder flow and laser heating in direct metal laser sintering process. *Powder Technology* **2017**, *315*, 300 – 308.
41. Ibarra-Medina, J.; Pinkerton, A. A numerical investigation of powder heating in coaxial laser metal deposition. Proceedings of the 36th International MATADOR Conference. Springer, London, 2010. doi:https://doi.org/10.1007/978-1-84996-432-6_101.
42. Pan, H.; Sparks, T.; Thakar, Y.D.; Liou, F. The Investigation of Gravity-Driven Metal Powder Flow in Coaxial Nozzle for Laser-Aided Direct Metal Deposition Process. *J.Manuf.SCi.Eng.* **2005**, *128*, 541 – 553.
43. Zeng, Q.; Tian, Y.; Xu, Z.; Qin, Y. Numerical modelling of the gas-powder flow during the laser metal deposition for additive manufacturing. Proceedings of the 15 International COnference on Manufacturing Research, 2017.
44. Morimoto, K.; Suzuki, Y.; Kasagi, N. Mechanism of Heat Transfer Enhancement in Recuperators with Oblique Wavy Walls. *Thermal Science and Engineering* **2004**, *12*, 99–100.
45. Riella, M.; Kahraman, R.; Tabor, G. Reynolds-Averaged Two-Fluid Model prediction of moderately dilute fluid-particle flow over a backward-facing step. *International Journal of Multiphase Flow* **2018**, *106*, 95 – 108. doi:https://doi.org/10.1016/j.ijmultiphaseflow.2018.04.014
46. Riella, M.; Kahraman, R.; Tabor, G. Inhomogeneity and anisotropy in Eulerian–Eulerian near-wall modelling. *International Journal of Multiphase Flow* **2019**, *114*, 9 – 18. doi:https://doi.org/10.1016/j.ijmultiphaseflow.2019.01.014.

47. van Wachem, B.V.A.N. Derivation, implementation, and validation of computer simulation models for gas-solid fluidized beds, 2000.
48. Geldart, D. Types of gas fluidization. *Powder Technology* **1973**, *7*, 285–292. doi:10.1016/0032-5910(73)80037-3.
49. Gidaspow, D.; Huilin, L. Equation of State and Radial Distribution Functions of FCC Particles in a CFB. *AIChE Journal* **1998**, *44*, 279–293.
50. Van Wachem, B.; Sasic, S. Derivation, simulation and validation of a cohesive particle flow CFD model. *AIChE Journal* **2008**, *54*, 9–19. doi:10.1002/aic.11335.
51. Ocone, R. Goodwin, J.; Delebarre, A. Flow structures of Geldart A solids in circulating fluidized beds. *Trans IChemE* **2000**, *78*, 860–865.
52. Makkawi, Y.T.; Wright, P.C.; Ocone, R. The effect of friction and inter particle cohesive forces on the hydrodynamics of gas solid flow. A comparative analysis of theoretical predictions and experiments. *Powder Technology* **2006**, *163*, 69–79. doi:10.1016/j.powtec.2006.01.020.
53. Lingard, W.; Stone, A. LPW Powder Evaulation Report for AlSi10Mg, Sample 2737, 15th April 2016, 2016.
54. Lingard, W.; Stone, A. LPW Powder Evaulation Report for Inconel 625, Batch UK82252, 21st December 2017, 2017.
55. Vlachos, N.; Chang, I.T.H. Investigation of flow properties of metal powders from narrow particle size distribution to polydisperse mixtures through an improved Hall flowmeter. *Powder Technology* **2011**, *205*, 71–80. doi:10.1016/j.powtec.2010.08.067.
56. Kamenetskii, E.S.; Orlova, N.S.; Tagirov, A.M.; Volik, M.V. Three-Dimensional Simulation of a Vibrofluidized Bed with the Use of a Two-Fluid Model of Granular Gas. *Journal of Engineering Physics and Thermophysics* **2016**, *89*, 1459–1465. doi:10.1007/s10891-016-1514-5.
57. Richman, M.W. Boundary conditions for granular flows at randomly fluctuating bumpy boundaries. *Mechanics of Materials* **1993**, *16*, 211–218.
58. Viswanathan. Convection in three-dimensional vibrofluidized granular beds. *Journal of Fluid Mechanics* **2011**, *682*, 185–212. doi:10.1017/jfm.2011.209.
59. Orlova, N.S. Comparison of the results of experimental investigations of a vibrofluidized bed with caluclations by a granular gas hydrodynamic model. *Journal of Engineering Physics and Thermophysics* **2014**, *87*, 429–435.
60. Morimoto, K.; Suzuki, Y.; Kasagi, N. Optimal Shape Design of Compact Heat Exchangers based on Adjoint Analysis of Momentum and Heat Transfer. *Journal of Thermal Science and Technology* **2010**, *5*, 24 – 35.
61. Kahraman, R.; Bacheva, D.; Schmieder, A.; Tabor, G.R. Coupling of Volume of Fluid and Level Set Methods in Condensing Heat Transfer Simulations. *Int.J.CFD* **2019**. doi:10.1080/10618562.2019.1693546.
62. Gledhill, I.M.A.; Roohani, H.; Forsberg, K.; Eliasson, P.; Skews, B.W.; Nordström, J. Theoretical treatment of fluid flow for accelerating bodies. *Theoretical and Computational Fluid Dynamics* **2016**, *30*, 449–467. doi:10.1007/s00162-016-0382-0.
63. Matsusaka, S.; Yamamoto, K.; Masuda, H. Micro-feeding of a fine powder using a vibrating capillary tube. *Advanced Powder Technology* **1996**, *7*, 141–151. doi:10.1016/S0921-8831(08)60509-9.
64. Kroll, V.W. Uber das Verhalien yon Schiittgut in lotrecht schwingenden Gef iBen. *Forschung* **1953**, pp. 2–15.